# Supporting information:
# Enhancing the electronic dimensionality of hybrid organic-inorganic frameworks by hydrogen bonded molecular cations

Fedwa El-Mellouhi [*a], Mohamed E. Madjet [a], Golibjon R. Berdiyorov [a], El Tayeb Bentria [a], Sergey N. Rashkeev [a], Sabre Kais[c] , Akinlolu Akande [e], Carlo Motta [d], Stefano Sanvito [d], and Fahhad H.AlHarbi [a,b]

[a] Qatar Environment and Energy Research Institute, Hamad bin Khalifa University, P. O. Box 34110, Doha, Qatar.
[b] College of Science and Engineering, Hamad Bin Khalifa University, Doha, Qatar.
[c] Department of Chemistry, Physics, and Birck Nanotechnology Center, Purdue University, West Lafayette, Indiana 47907, USA.
[d] School of Physics, AMBER and CRANN Institute, Trinity College, Dublin 2, Ireland.
[e]School of Science, Institute of Technology, Ash Lane, Sligo, Ireland
[*]felmellouhi@hbku.edu.qa

## Computational details

### 1. Geometry optimization and electronic structure calculations

The geometric optimization was performed using the Vienna Ab Initio Simulation Package (VASP) [1], [2] using the density functional theory (DFT) within the generalized gradient approximation of Perdew-Burke-Ernzerhof (PBE) for the exchange-correlation energy [3]. Non-bonded van der Waals interactions are accounted for using Grimme's PBE empirical correction.The projector augmented wave (PAW) pseudopotentials were used with a cutoff energy of 520 eV. Monkhorst-Pack *k*-point sampling method is used for the Brillouin zone integration. The structures were fully relaxed using the Conjugate-Gradient algorithm until reaching $10^{-4}$ eV/Å convergence criterion for the Hellman-Feynman forces. The deformation potential, dielectric function and optical phonon frequency were calculated using VASP as well. The deformation potential was calculated flowing the approach of Ref. [8] and the dielectric function was calculated using 12×6×12 –k-point mesh and $10^{-12}$ energy difference tolerance. Due to the flat band curvature characterizing these low dimensional materials, automated extraction of the effective masses is sometimes challenging. Therefore, the effective masses were extracted manually for vanadates along the three crystallographic directions as demonstrated in figure S1. The polynomial fitting was of order 4, we used 6th order for some flat bands for better fitting.

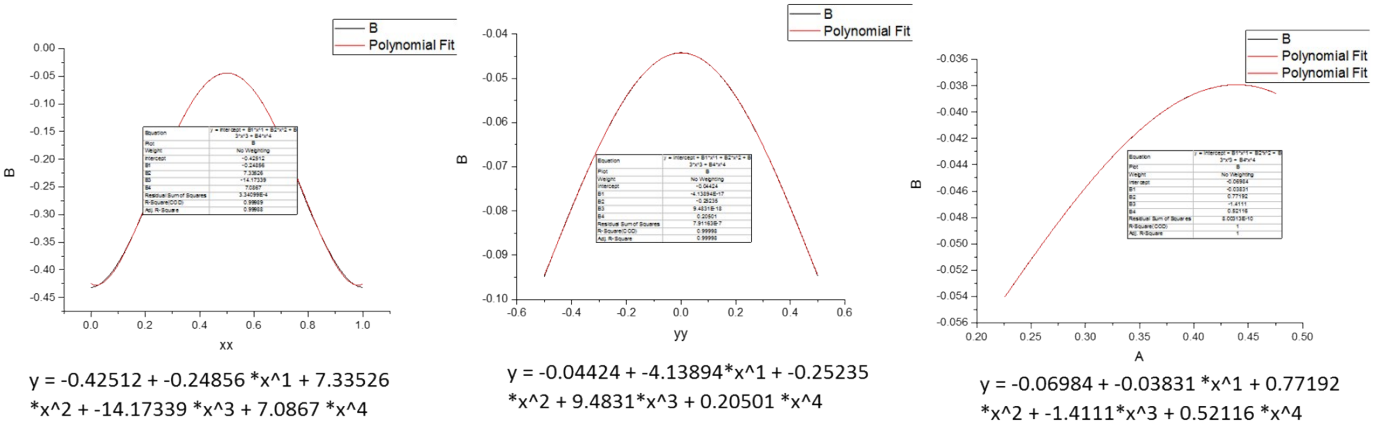


Figure S1: Examples of the effective mass calculation for holes in $NH_4VO_3$ by solving the derivative of polynomial fitting function.

### 2. Electronic transport and scattering time calculations

Abinit, BoltzTrap and the newly released Boltztrap2 packages has been conducted used to calculate the thermoelectric properties [4,5]. Boltztrap2 and Abinit have been used to calculate the mobility beyond the constant relaxation time approximation and BoltzTrap for its capability to calculate mobility in the three directions. Boltztrap2 uses "all bands fitting method" to accurately calculate the mobility taking into account the electron-phonon scattering effect. This is

possible by reading a generated Abinit file containing the electron-phonon relaxation time as function of k-points ($\iota_k$ file) [6]. For group velocity determination in Boltztrap2, the band energies were supplied from VASP output. In order to minimize the error of band crossing and increase band fitting accuracy around the (CBM, VBM), we used a k-point mesh around 32×16×32 (i.e., 3375 k-points in the irreducible Brillouin zone) which is sufficient mesh considering the large volume of the computational unit cells (more than 350 Å$^3$). A convergence study has been made with respect to k-point sampling.

The electron-phonon couplings were obtained using the ABINIT software package [6]. Since the relaxation time calculations are very sensitive to the calculation parameters such as pseudopotentials and the integration methods, we used the latest version of psp8 pseudo potential [7], which is highly recommended for phonon calculations. The low symmetry of the metavanadates together with the high number of atoms per cell (864 perturbation for $NH_4VO_3$ for example) make the calculation computationally demanding. Therefore, we use 8×8×8 k-point mesh together with a 2×2×2 q-point grid, a Fermi surface smearing of 0.01 Ha, a cut-off energy of 20 Ha. These calculations generate more than 6 GB matrix element files to be analyzed by ***anaddb*** post processing tool and extract the relaxation time [8,9].

## 3. Ballistic charge transport

The electronic transport calculations are performed using the computational package Atomistix toolkit [10].Optimized geometries from the VASP calculations (i.e., lattice parameters and atomic positions) are used to perform electronic transport calculations using DFT in combination with the Green's functional formalism. The electronic structure is calculated self-consistently within the DFT/PBE and the electrostatic potential is obtained on a real-space grid with a density mesh cutoff energy of 2000 eV. Double-zeta-polarized basis sets of local numerical orbitals are used for all atoms.

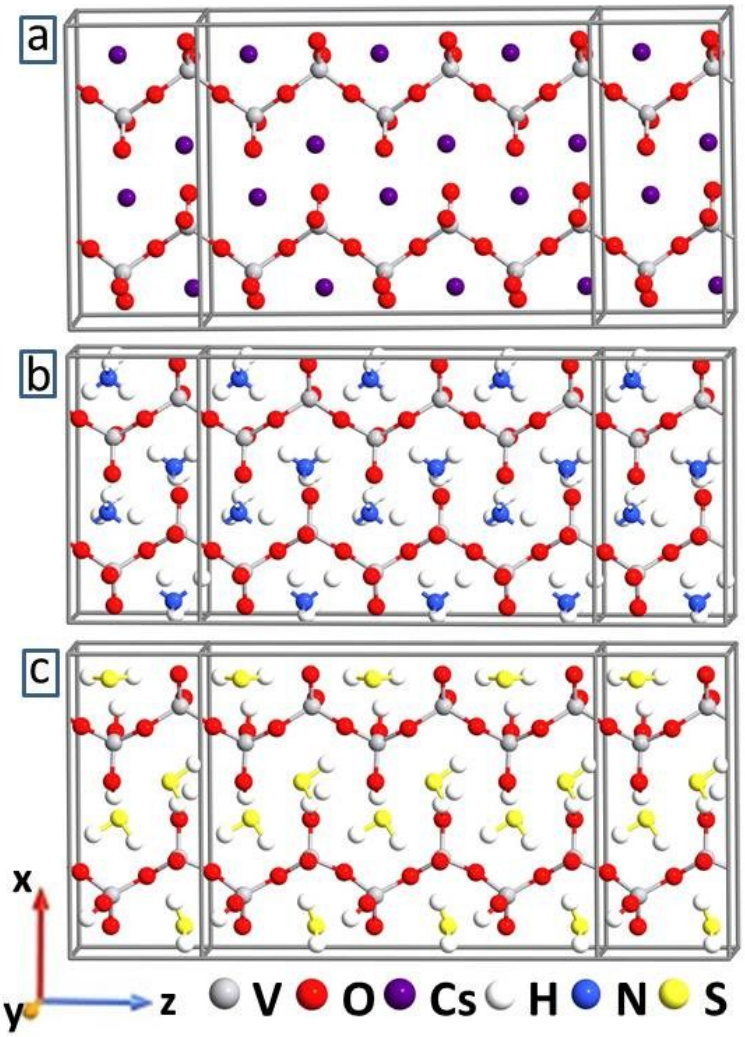


Figure S2. Two probe device geometries made from $CsVO_3$ (a), $NH_4VO_3$ (b) and $H_3SVO_3$ (c). Periodic boundary conditions are used along the x- and y-directions and transmission is calculated along the z-direction through the metallic electrodes.

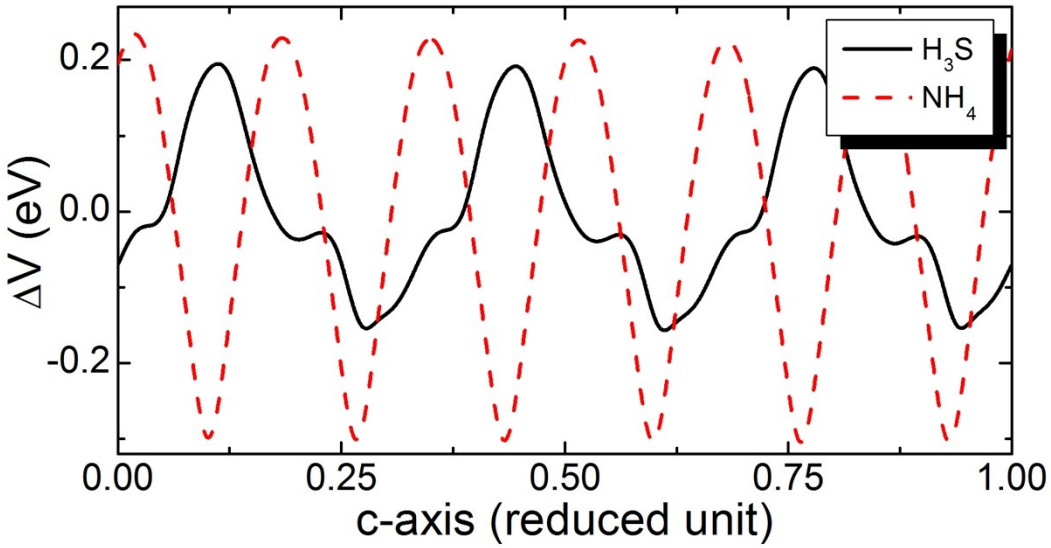


Figure S3. Electrostatic potential variations along the transport direction for $H_3SVO_3$ (solid curve) and $NH_4VO_3$ (dashed curve) samples.

## 4. Hot carrier relaxation dynamics

The non-adiabatic molecular dynamics (NAMD) simulations are conducted using the PYthon eXtension for Ab Initio Dynamics (PYXAID) package [11,12,13] . The calculations are performed in three steps. First, the considered systems are geometry optimized with VASP and using PBE functional and projector augmented-wave pseudopotentials. After that, ab initio MD simulations are performed for 5 ps in the canonical NVT ensemble. The velocity Verlet algorithm with a time step of 1 fs is used to propagate the nuclear coordinates, and a shorter time of 0.1 fs is used to propagate the electronic amplitudes. In the second step, the electronic structure of the considered systems is recomputed for each time step along the molecular dynamics trajectory. The computed Kohn-Sham (KS) orbitals and energies are utilized to get the non-adiabatic couplings (NAC) and the transition dipole matrix elements to form the vibronic Hamiltonian matrix. This time-dependent information is stored and used to perform the subsequent NAMD simulations and data analysis. Note that for the excited state dynamics, only the Gamma point of the Brillouin zone is used. In the third step, the NAMD simulations are performed. In order to study hot carriers relaxations dynamics, we have chosen a minimal basis of the adiabatic excited states represented by excited Slater determinants constructed from the KS orbitals. In order to get reliable statistics, the results are averaged over 1000 stochastic realizations of the surface hopping algorithms and 20 starting geometries. Non-adiabatic transitions from the eight lowest excited states were included in the calculation of electron and hole relaxation dynamics. Finally, the analysis was performed only on the trajectories of 2 ps after an equilibration phase of 1ps.

## Optical properties

Figure S4 shows the absorption spectrum of the considered systems as a function of photon energy. For the range of the photon energy between 1.5 and 2.81 eV, the $H_3SVO_3$ shows higher absorption in the visible range of the spectrum (~ 1.5 – 3.0 eV) than other considered materials.

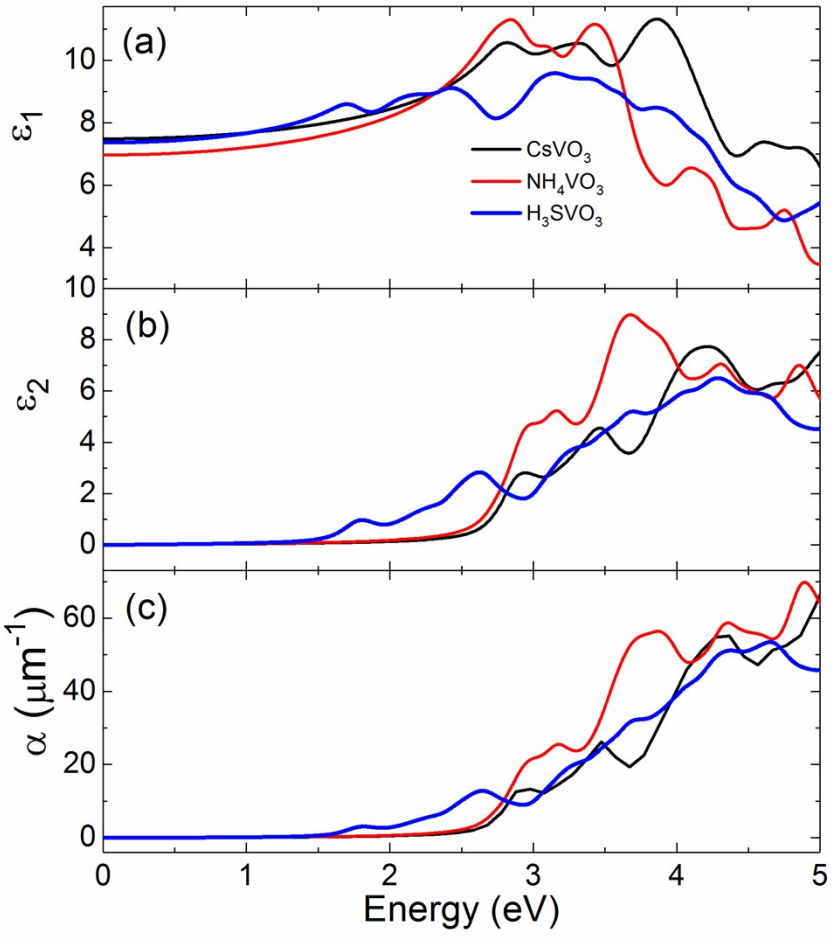


Figure S4: Calculated real (a) and imaginary (b) parts of the dielectric function and absorption spectra (c) as a function of photon energy for $CsVO_3$ (black curves) $NH_4VO_3$ (red curves) and $H_3SVO_3$ (blue curves).

**Additional simulation results**

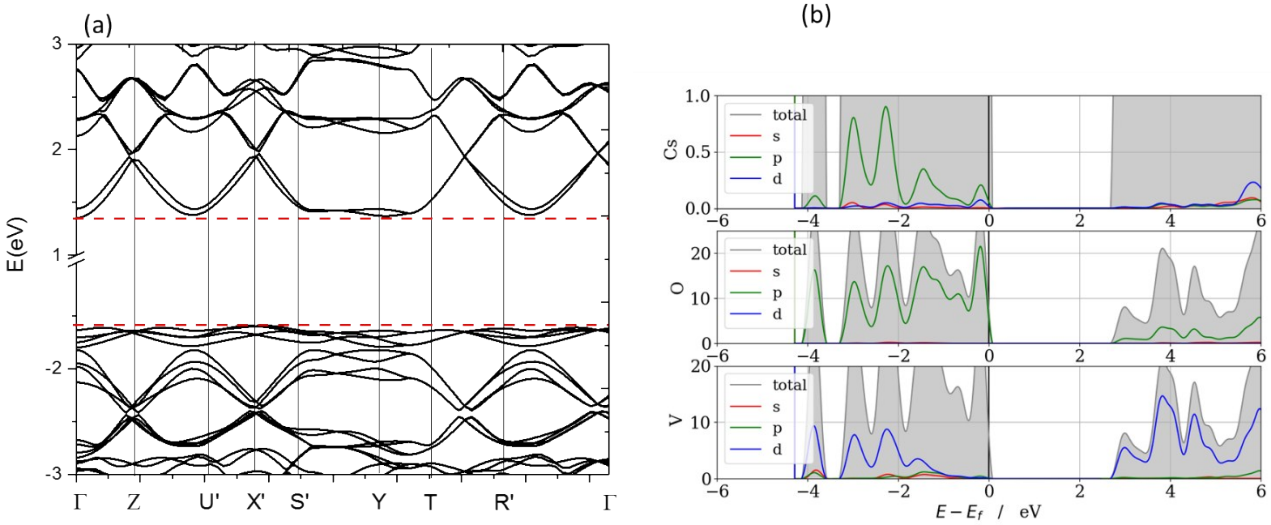


Figure S5 : (a) Electronic band structure and (b) total (gray shadow) and site projected density of state for $CsVO_3$.

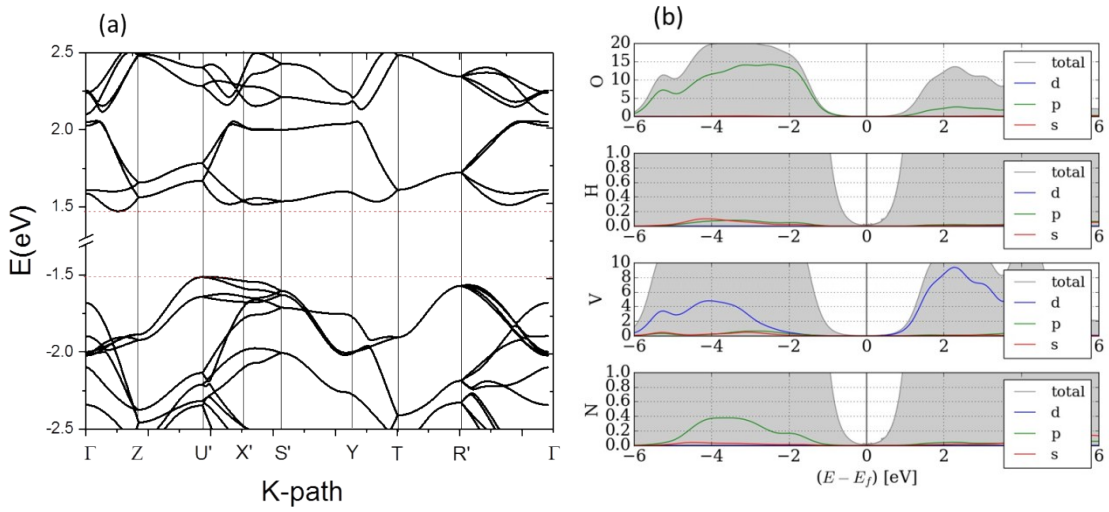


Figure S6 : (a) Electronic band structure and (b) total (gray shadow) and site projected density of state for $NH_4VO_3$.

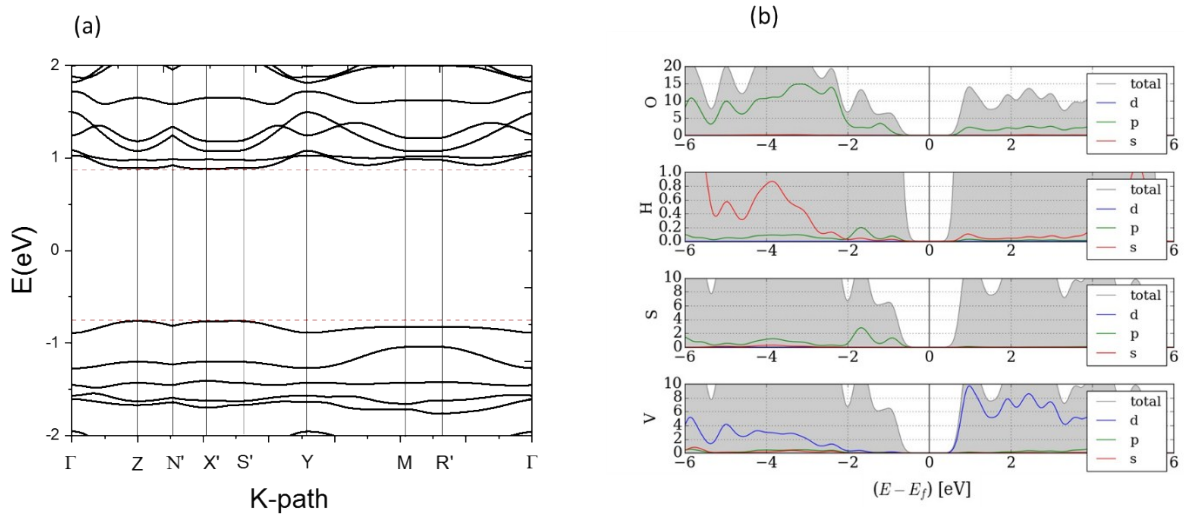


Figure S7: (a) Electronic band structure and (b) total (gray shadow) and site projected density of state for H3SVO3.

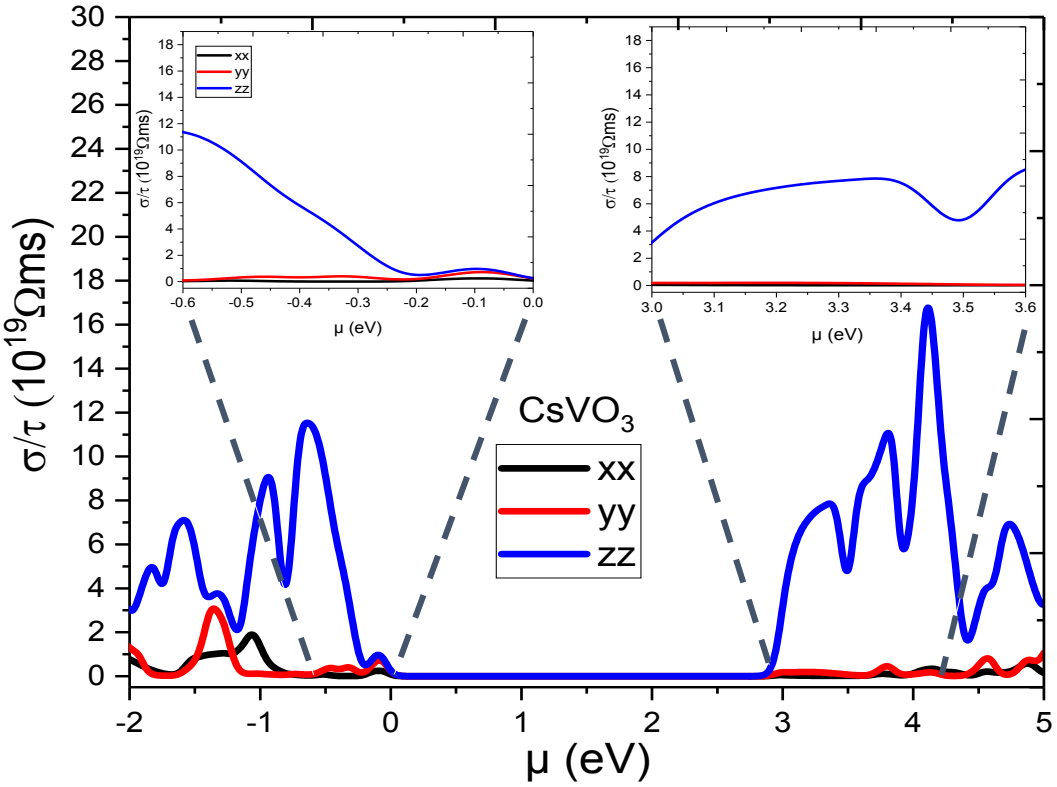


Figure S8: Conductivity over relaxation time (σ/τ) tensor as a function of chemical potential μ for $CsVO_3$with a zoom-in to the region ±0.5eV of band gap, in order to present in detail the responsible directions of thermoelectric properties.

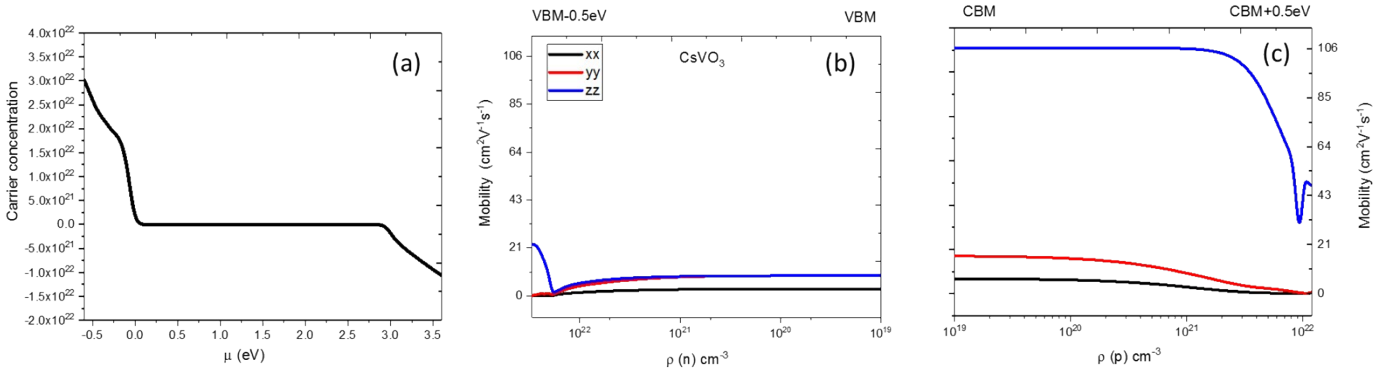


Figures S9: (a) Electron concentration of $CsVO_3$ as a function of the chemical potential around the band gap (±0.5 eV off CBM/VBM). (b,c) Mobility tensors of $CsVO_3$ as a function of the charge concentration (ρ) for *hole* (h) and *electron (n)* in the three Cartesian directions. Mobility is calculated using Boltztrap with to mean relaxation time calculated using Abinit.

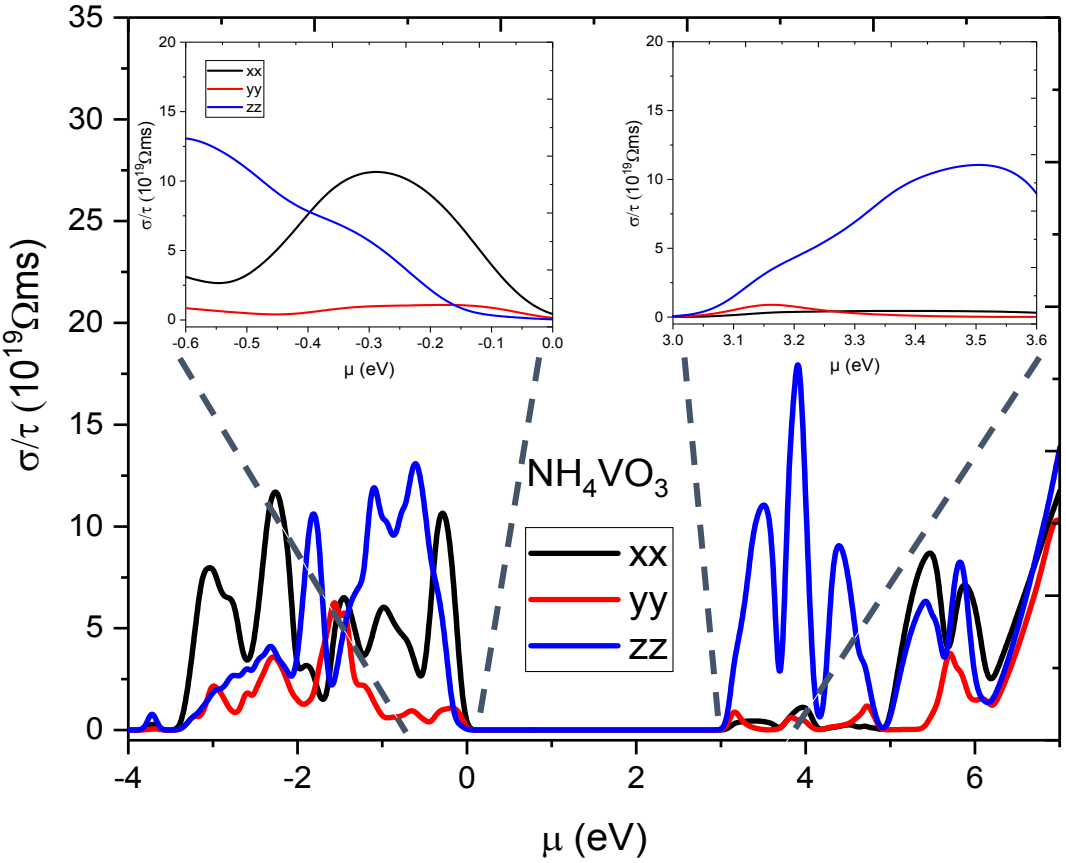


Figure S10: Conductivity over relaxation time (σ/τ) tensor as a function of chemical potential μ for $NH_4VO_3$with a zoom-in to the region ±0.5eV of band gap, in order to present in detail the responsible directions of thermoelectric properties.

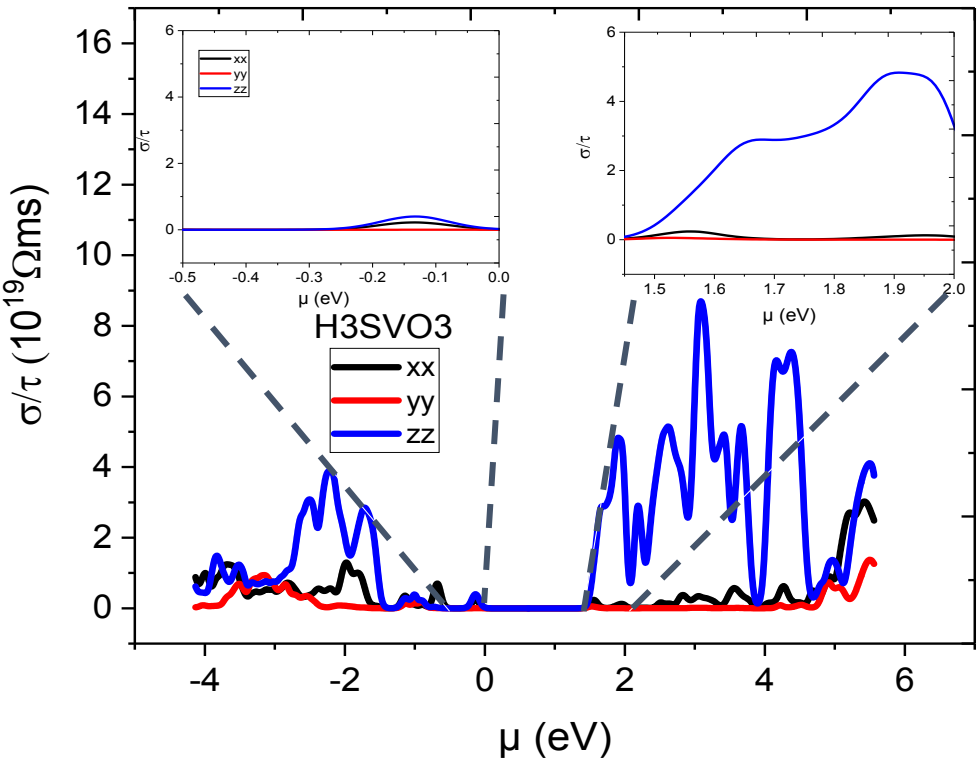

Figure S11: Conductivity over relaxation time (σ/τ) tensor as a function of chemical potential μ for $H_3SVO_3$with a zoom-in to the region ±0.5eV of band gap, in order to present in detail the responsible directions of thermoelectric properties.

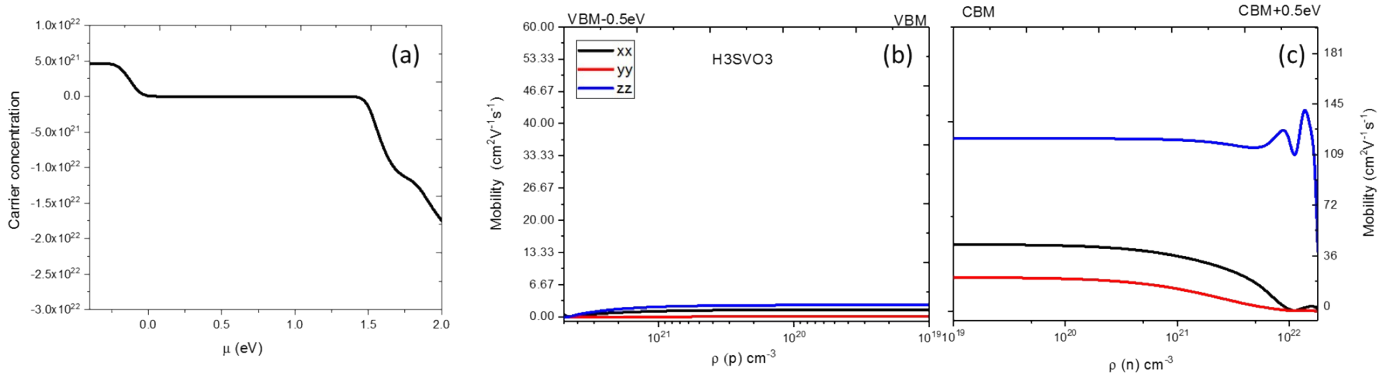


Figures S12: (a) Electron concentration of $H_3SVO_3$ as a function of the chemical potential around the band gap (±0.5 eV off CBM/VBM). (b,c) Mobility tensors of $H_3SVO_3$ as a function of the charge concentration (ρ) for *hole* (h) and *electron (n)* in the three Cartesian directions. Mobility is calculated using Boltztrap with to mean relaxation time calculated using Abinit.

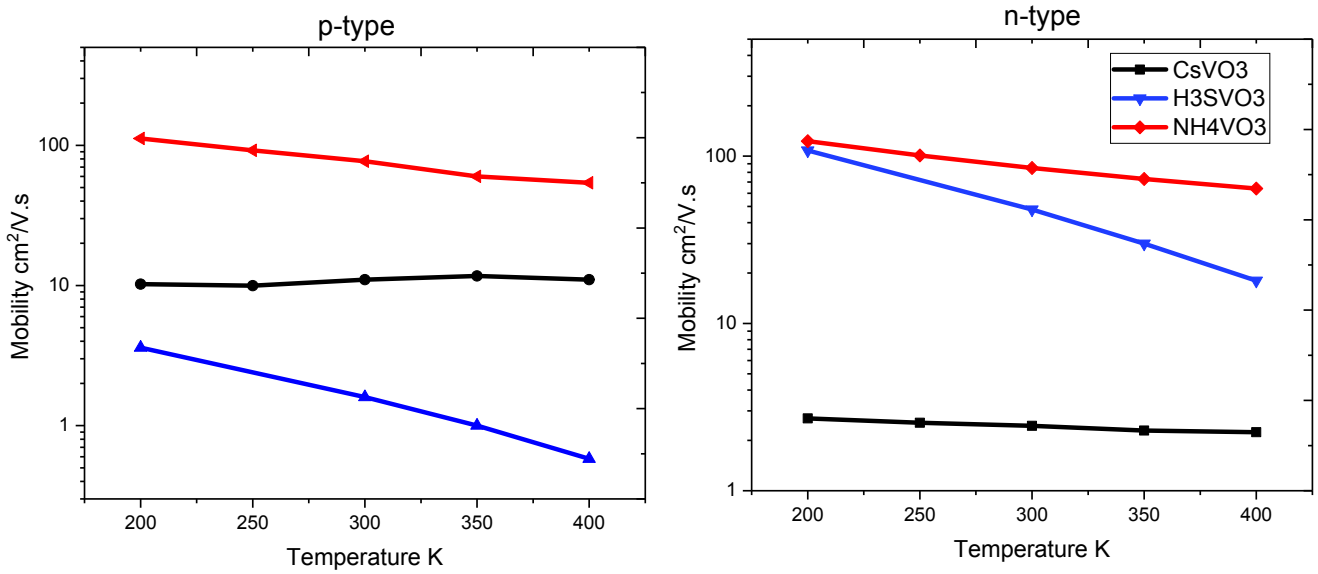


Figure S13: Carrier mobility as function of temperature for of $CsVO_3$ (black), $NH_4VO_3$ (red) and $H_3SVO_4$ (blue), for a carrier concentration of $10^{18}$ $cm^{-3}$.

| **Property** | **$CsVO_3$** | **$H_3SVO_3$** | **$NH_4VO_3$** |
|---|---|---|---|
| **Static dielectric** | 2.87 | 3.38 | 3.37 |
| **High frequency dielectric** | 2.88 | 3.52 | 3.37 |
| **Deformation potential (n/p) type** | 8.23/4.65 | 8.7/6.6 | 9.75/6.16 |
| **Polar Optical phonon frequency ($cm^{-1}$ )** | 28.44 | 93.69 | 97.40 |
| **Calculated (electron/hole) effective masses** | 0.26/0.34 | 1.06/0.20 | 0.77/0.36 |

Table S1: Calculated static and high frequency dielectric constant, n/p type deformation potentials, polar phonon (PO) band frequency and electron/hole effective masses for the compounds analyzed in this work.

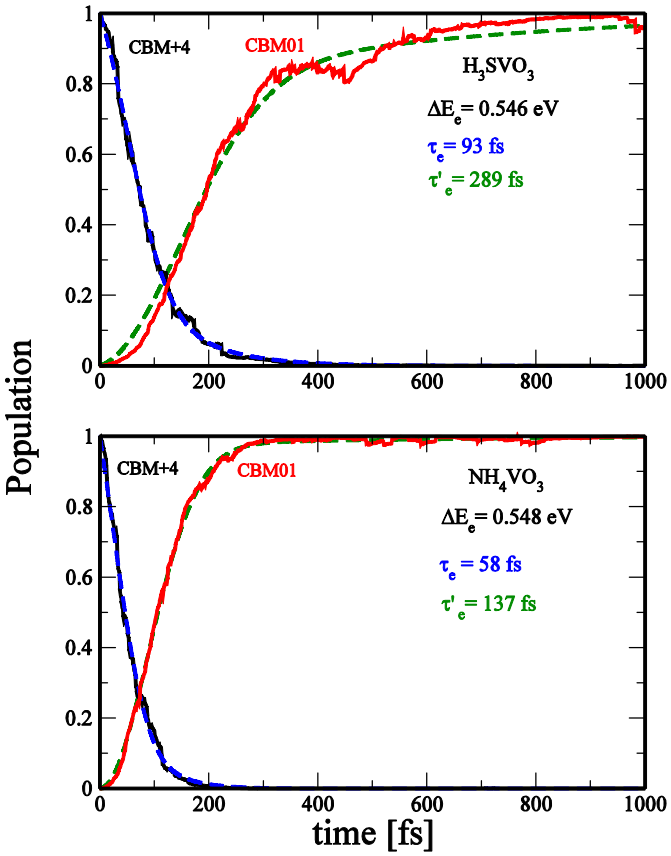


Figure S14. Electron population decay after initial excitation to the excited state CBM+4 for $H_3SVO_3$ and $NH_4VO_3$. The electron population of the lowest two electronic states CBM01 (Pop(CBM01)=Pop(CBM) + Pop(CBM+1)) is also shown.

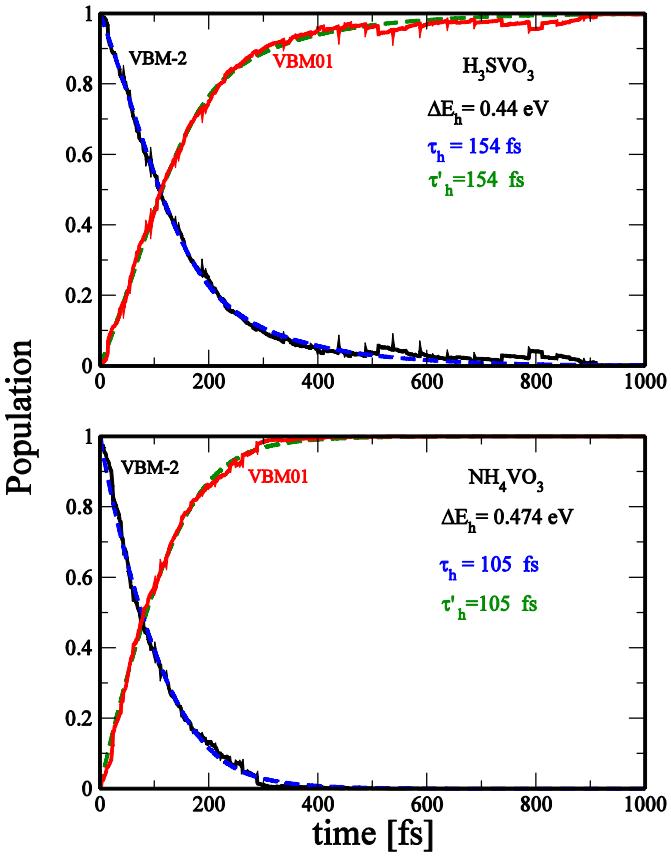


Figure S15. Hole population decay after initial excitation to the excited state (VBM-2) for $H_3SVO_3$ (top panel) and $NH_4VO_3$ (bottom panel). The hole population of the lowest two electronic states VBM01 (Pop(VBM01)=Pop(VBM) + Pop(VBM-1)) is also shown.

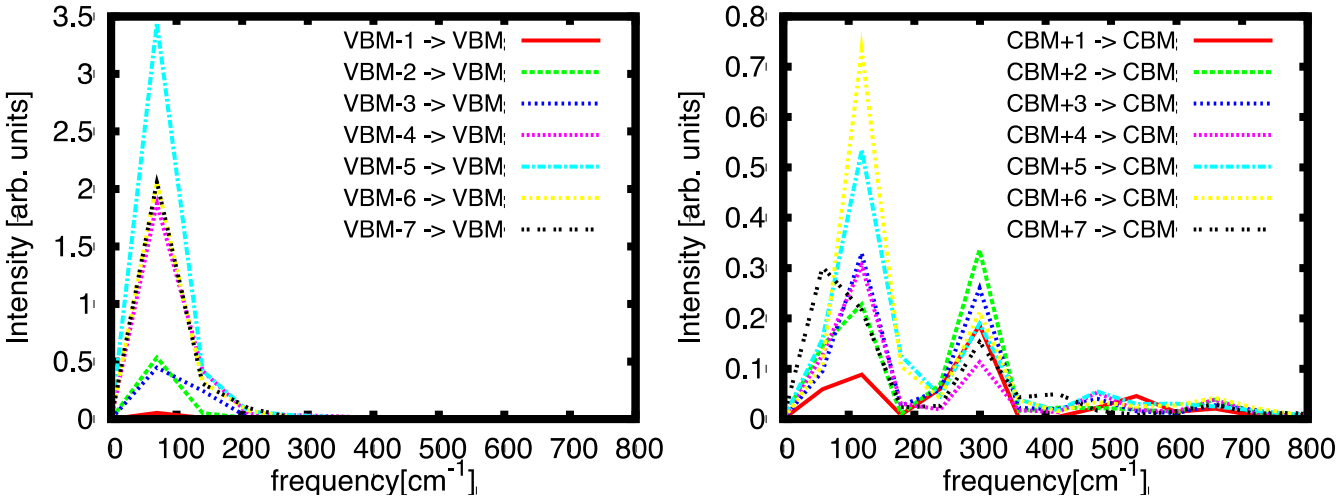


Figure S16 Phonon modes driving the hole (left) and electron (right) relaxations for $H_3SVO_3$ without convolution.

| **ρ ($cm^{-3}$)** | **$\mu_{ave}$ (in $cm^2/V.s$)** | | |
|---|---|---|---|
| | $CsVO_3$ | $NH_4VO_3$ | $H_3SVO_3$ |
| **1.00E+13** | 7.9 | 101.7 | 6.3 |
| **1.00E+14** | 9.7 | 127.3 | 19.9 |
| **1.00E+15** | 9.9 | 129.6 | 25.2 |
| **1.00E+16** | 10.0 | 130.4 | 24.8 |
| **1.00E+17** | 10.0 | 130.5 | 24.8 |
| **1.00E+18** | 10.0 | 130.5 | 24.8 |
| **1.00E+19** | 9.9 | 129.3 | 24.8 |
| **1.00E+20** | 9.8 | 122.9 | 25.3 |
| **1.00E+21** | 6.0 | 92.6 | 26.6 |

Table S2: Calculated total, electron and holes average mobility $\mu_{ave}$ in ($cm^2/V.s$) as function of the charge concentration (ρ) in the $n_e = n_p$ injected regime at 300K, for $CsVO_3$, $NH_4VO_3$ and $H_3SVO_3$.

| **ρ ($cm^{-3}$)** | **D ($cm^2/s$)** | | |
|---|---|---|---|
| | $CsVO_3$ | $NH_4VO_3$ | $H_3SVO_3$ |
| **1.00E+13** | 0.203 | 2.612 | 0.164 |
| **1.00E+14** | 0.251 | 3.269 | 0.512 |
| **1.00E+15** | 0.256 | 3.330 | 0.648 |
| **1.00E+16** | 0.257 | 3.349 | 0.638 |
| **1.00E+17** | 0.257 | 3.353 | 0.638 |
| **1.00E+18** | 0.257 | 3.352 | 0.637 |
| **1.00E+19** | 0.256 | 3.321 | 0.638 |
| **1.00E+20** | 0.252 | 3.157 | 0.651 |
| **1.00E+21** | 0.156 | 2.380 | 0.685 |

Table S3: Average carrier diffusion coefficients D ($cm^2/s$) calculated at room temperature as function carrier concentration for electrons and holes in ($n_e = n_p$) charge density regime.

| ρ ($cm^{-3}$) | $L_D^{min}$(m) | | |
|---|---|---|---|
| | $CsVO_3$ | $NH_4VO_3$ | $H_3SVO_3$ |
| **1.00E+13** | 1.43E-07 | 5.24E-07 | 3.00E-07 |
| **1.00E+14** | 1.58E-07 | 5.86E-07 | 5.31E-07 |
| **1.00E+15** | 1.6E-07 | 5.91E-07 | 5.97E-07 |
| **1.00E+16** | 1.6E-07 | 5.93E-07 | 5.92E-07 |
| **1.00E+17** | 1.6E-07 | 5.93E-07 | 5.92E-07 |
| **1.00E+18** | 1.6E-07 | 5.93E-07 | 5.92E-07 |
| **1.00E+19** | 1.6E-07 | 5.91E-07 | 5.92E-07 |
| **1.00E+20** | 1.59E-07 | 5.76E-07 | 5.98E-07 |
| **1.00E+21** | 1.25E-07 | 5.00E-07 | 6.14E-07 |

Table S4: Total calculated carrier diffusion lengths $L_D^{min}$ (in meter) as function of carrier concentration with ($n_e = n_p$) injected densities at 300K.

## References


[1] G. Kresse and J. Furthmüller, "Efficient iterative schemes for ab initio total-energy calculations using a plane-wave basis set," *Phys. Rev. B*, vol. 54, no. 16, p. 11169, 1996.

[2] G. Kresse and J. Hafner, "No Title," *Phys. Rev. B*, vol. 47, p. 558, 1993.

[3] J. P. Pedrew, K. Burke, and M. Ernzerhof, *Phys. Rev. Lett.*, vol. 77, p. 3865, 1996.

[4] G. K. H. Madsen and D. J. Singh, "BoltzTraP. A code for calculating band-structure dependent quantities," Comput. Phys. Commun., vol. 175, no. 1, pp. 67–71, 2006.

[5] G. K. H. Madsen, J. Carrete, and M. J. Verstraete, "BoltzTraP2, a program for interpolating band structures and calculating semi-classical transport coefficients," arXiv Prepr. arXiv1712.07946, 2017.

[6] X. Gonze, F. Jollet, F. A. Araujo, D. Adams, B. Amadon, T. Applencourt, C. Audouze, J.-M. Beuken, J. Bieder, and A. Bokhanchuk, "Recent developments in the ABINIT software package," Comput. Phys. Commun., vol. 205, pp. 106–131, 2016.

[7] D. R. Hamann, "Optimized norm-conserving Vanderbilt pseudopotentials," Phys. Rev. B, vol. 88, no. 8, p. 85117, 2013.

[8] M. D. Matthieu Verstraete, Bin Xu, "Abinit electron phonon interaction calculations for geniuses," 2006. https://docs.abinit.org/topics/documents/elphon_manual.pdf

[9] A. Filippetti, A. Mattoni, C. Caddeo, M. I. Saba, and P. Delugas, "Low electron-polar optical phonon scattering as a fundamental aspect of carrier mobility in methylammonium lead halide CH 3 NH 3 PbI 3 perovskites," Phys. Chem. Chem. Phys., vol. 18, no. 22, pp. 15352–15362, 2016.

[10] S. QuantumWise and S. ATK e-manual, "Atomistix ToolKit, version 2016.3," Synopsys QuantumWise, Copenhagen Google Sch., 2016.

[11] A. V Akimov and O. V Prezhdo, "The PYXAID program for non-adiabatic molecular dynamics in condensed matter systems," J. Chem. Theory Comput., vol. 9, no. 11, pp. 4959–4972, 2013.

[12] M.E. Madjet, A.V. Akimov, F. El-Mellouhi, G.R. Berdiyorov, S. Ashhab, N. Tabet and S. Kais, Enhancing the carrier thermalization time in organometallic perovskites by halide mixing, Phys. Chem. Chem. Phys., 2016,18, 5219-5231.

[13] M. E. Madjet, G. R Berdiyorov, F. El-Mellouhi, F. H. Alharbi, A. V. Akimov and Sabre Kais, Cation Effect on Hot Carrier Cooling in Halide Perovskite Materials, J. Phys. Chem. Lett.. 2017, 8, 4439-4445.